Published in final edited form as:
Nanomedicine (Lond). 2014 June ; 9(8): 1181–1192. doi:10.2217/nnm.13.72.

Rapid dramatic alterations to the tumor microstructure in pancreatic cancer following irreversible electroporation ablation

Zhuoli Zhang[1,2], **Weiguo Li**[1], **Daniel Procissi**[1], **Patrick Tyler**[1], **Reed A Omary**[1,2,3], and **Andrew C Larson**[*,1,2,3]

[1]Department of Radiology, Northwestern University, 737 N. Michigan Avenue, 16th Floor, Chicago, IL 60611, USA

[2]Robert H Lurie Comprehensive Cancer Center, Northwestern University, 737 N. Michigan Avenue, 16th Floor, Chicago, IL 60611, USA

[3]Department of Biomedical Engineering, Northwestern University, 2145 Sheridan Road, Evanston, IL 60208, USA

Abstract

Aim—NanoKnife® (Angiodynamics, Inc., NY, USA) or irreversible electroporation (IRE) is a newly available ablation technique to induce the formation of nanoscale pores within the cell membrane in targeted tissues. The purpose of this study was to elucidate morphological alterations following 30 min of IRE ablation in a mouse model of pancreatic cancer.

Materials & methods—Immunohistochemistry markers were compared with diffusion-weighted MRI apparent diffusion coefficient measurements before and after IRE ablation.

Results—Immunohistochemistry apoptosis index measurements were significantly higher in IRE-treated tumors than in controls. Rapid tissue alterations after 30 min of IRE ablation procedures (structural and morphological alterations along with significantly elevated apoptosis markers) were consistently observed and well correlated to apparent diffusion coefficient measurements.

Discussion—This imaging assay offers the potential to serve as an *in vivo* biomarker for noninvasive detection of tumor response following IRE ablation.

Keywords

apoptosis; irreversible electroporation; MRI biomarker; NanoKnife®; pancreatic cancer; therapy response

*Author for correspondence: Tel.: +1 312 926 3499, Fax: +1 312 926 5991, a-larson@northwestern.edu.

Financial & competing interests disclosure
The authors have no other relevant affiliations or financial involvement with any organization or entity with a financial interest in or financial conflict with the subject matter or materials discussed in the manuscript apart from those disclosed.
No writing assistance was utilized in the production of this manuscript.

Ethical conduct of research
The authors state that they have obtained appropriate institutional review board approval or have followed the principles outlined in the Declaration of Helsinki for all human or animal experimental investigations. In addition, for investigations involving human subjects, informed consent has been obtained from the participants involved.

Pancreatic ductal adenocarcinoma (PDAC), the fourth leading cause of US cancer-related mortality, carries the worst prognosis of any cancer. Of the patients with PDAC, 99% will die of their disease; median survival is 6 months and 5-year survival is <5%. Surgical resection, the only potentially curative measure, is possible in <20% of cases and of these patients, median 5-year survival is only 10% [1,2]. Disruptive approaches are critically needed to impact this deadly disease.

Locoregional therapies for solid tumors have gained traction over the past decade as a way to improve patient survival, downstage a patient to a curative surgical procedure, or palliate patients with incurable disease [3–5]. These targeted approaches are typically less toxic and less invasive than chemotherapy or surgical procedures [3–5]. Several ablation techniques have been developed, including cryoablation, radiofrequency ablation and microwave ablation [6–13]. Isolated or in combination, these techniques can improve patient survival or provide a highly effective option for palliative care [3,14,15].

In 2005, tissue ablation with irreversible electroporation (IRE) was introduced for cancer therapy [16]. IRE is a newly available ablation technique involving the application of short, intense bursts of electrical energy to induce the formation of nanoscale pores within the membrane of cells in targeted tissues with minimal deposition of thermal energy [17,18]. Multiple studies have previously demonstrated that cells within the IRE-treated tissues ultimately enter coagulative necrosis and the apoptotic cell death pathway [13,19–21]. IRE disrupts cellular physiology, producing nearly complete cell kill within the targeted areas of ablation [22]. Preclinical studies in subcutaneous tumor models, human cancer cells, normal liver and liver-implanted tumor tissues, and prostate tissues have each demonstrated the feasibility of using IRE as a new ablation option with negligible thermal side effects [14,19,23–25].

Scanning electron microscopy (SEM) studies in cell culture and normal tissues have demonstrated the formation of nanoscale pores within cell membranes following IRE ablation procedures, importantly confirming this anticipated structural impact [17,20]. However, SEM generally does not permit interrogation of subcellular alterations to internal structures (i.e., damage to the nucleus or organelles). Recently, damage to both nuclear and cellular membranes was observed using transmission electron microscopy (TEM) studies following electrochemotherapy in an ovarian cancer cell line [26]; similarly, TEM studies following electroporation in melanoma xenografts provided evidence that suggested fragmentation of cellular membranes [27]. To date, there have been no results regarding the quantitative estimation of tumor response based on a cellular level (tumor microenvironment), following IRE ablation.

Both TEM and immunohistochemistry (IHC) measurements should be valuable for investigating IRE-induced alterations to the tumor microstructure. These assays are particularly important for preclinical studies intended to elucidate mechanisms of therapeutic response. However, alternative, noninvasive methods to detect IRE-induced alterations to cell membrane integrity could be useful for *in vivo* preclinical and clinical studies intending to determine the serial time course of treatment response. Particularly in

clinical settings, the detection of early therapy response may be critical to prompt retreatment or adoption of alternative therapies when necessary. Biopsies can be sampled to provide tissue for follow-up histology and microscopy, but these are invasive procedures with associated pain and potentially serious complications. Alternatively, noninvasive MRI techniques are readily applicable in both preclinical and clinical settings. MRI measurements can be weighted to produce images with the resulting signal intensity dependent upon the Brownian motion (diffusion) of endogenous water within the imaged tissues. IRE-induced permeablization of cell membrane structures should remove barriers to water diffusion and diffusion-weighted (DW)-MRI might therefore serve as a noninvasive *in vivo* assay for detection of these alterations immediately following IRE ablation [28].

The purpose of our current study was to elucidate the subcellular morphological and structural alterations that occur following 30 min of IRE ablation and compare quantitative IHC markers of apoptosis with *in vivo* MRI measurements of endogenous water-mobility (diffusion) changes within the targeted tumor tissues. We performed NanoKnife® (Angiodynamics, Inc., NY, USA) ablation procedures in a mouse xenograft model of PDAC. TEM was used to examine ultrastructural modifications, and IHC measurements in treated and control tumors were compared with DW-MRI apparent diffusion coefficient (ADC) measurements before and after 30 min of IRE ablation.

Materials & methods

PDAC cell line & culture

The human PDAC cell line, PANC-1, was obtained commercially (American Type Culture Collection, MD, USA). This cell line was initially established from a human carcinoma of the exocrine pancreas. PANC-1 cells were grown in American Type Culture Collection-formulated DMEM with 10% fetal bovine serum at 37°C in a humidified atmosphere containing 5% CO_2. Before the implantation procedure, the viability of the cells was tested with Trypan blue staining, with a cell viability of >93% required for tumor implantation.

Mouse xenograft model of PDAC

All studies were approved by our Institutional Animal Care and Use Committee. Fourteen 6-week-old nude mice (Balb/c male mice, 13–17 g; Charles River, MA, USA) were used for these experiments. Early-passage PANC-1 cells were harvested, and 2×10^6 cells in 200 µl of phosphate-buffered saline were implanted into both flanks of each mouse, which reduced the number of animals in our study. A total of 3–4 weeks were allowed for tumor growth to a size of approximately 8 mm (longest diameter for each tumor measured using calipers) prior to IRE procedures. These mice were randomly divided into two groups: for the first group (n = 8), left-flank tumors went untreated while right-flank tumors were treated with IRE ablation protocol; for the second group (n = 6), both left and right flank tumors were treated with IRE ablation.

IRE ablation procedure

Animals were induced using a mixture of 2–3% isoflurane and 5 1/min oxygen via an automatic delivery system (isoflurane vaporizer, Vaporizer Sales and Services, GA, USA).

Animals were repeatedly monitored during the procedure for adequate anesthetic depth. The skin surface of the tumor area was shaved at the electrode sites. After baseline MRI (please see the 'MRI measurements' section), each mouse was fixed in a prone position within restraint apparatus. A BTX Electroporator (Model ECM830, Harvard Apparatus, MA, USA) was then used for IRE. Tweezertrodes™ (Harvard Apparatus) were used for these studies that include stainless steel circular disk electrodes (with a diameter of 11.5 mm) at each tip of the tweezer. Tweezer-style electrodes were placed in direct contact with the skin on opposite sides of the subcutaneous tumor. Next, a total of 64 100-μs-duration, 1250-V/cm square-wave pulses were applied with 100-ms spacing between pulses (the distance between calipers was adjusted to offering a 1250-kv/cm electric field for targeted tumor). These specific IRE timing parameters were chosen to achieve IRE of the tumor tissue while avoiding heating effects [29]. Immediately after the IRE procedure, animals were returned to the MRI scanner for follow-up imaging measurements.

MRI measurements

MRI studies were performed using a Bruker 7.0T ClinScan high-field small-animal MRI system (Bruker Biospin, Ettlingen, Germany) with a commercial mouse coil (Bruker Biospin). Body temperature was monitored continuously with a thermometer and controlled with a waterbed (SA Instruments, NY, USA). Following localization scans, T2-weighted anatomic images were acquired in both coronal and axial orientations to locate the tumors. Next, quantitative DW-MRI measurements were performed in axial orientation. Stejskal–Tanner DW spinecho sequence was used for DW-MRI measurements. The following parameters were used: field of view = 35 × 35 mm^2, matrix = 128 × 128, repetition time/echo time = 500/51.1 ms, slice thickness =1.0 mm, b-values = 0, 500 and 800 s/mm^2.

Postprocessing algorithms were implemented within the Matlab® 7.1 software package (Math-Works, MA, USA) to produce ADC maps. These were generated by voxel-wise fitting of the resulting signal intensities within the DW images to the Stejskal–Tanner equation 1:

$$\mathrm{Sb}=\mathrm{S}(0)\mathrm{e}-\mathrm{bADC} \quad \text{(Equation 1)}$$

where S(0) is the signal intensity in the absence of diffusion weighting and Sb is the signal intensity for those images acquired with diffusion-weighting [30]. For the ADC maps produced from both pre- and post-IRE MRI measurements, regions of interest were drawn to encompass the tumors and exclude surrounding tissue (single regions of interest drawn for each tumor at slice position axially bisecting tumor). ADC values for the tumors at pre- and post-IRE time points were recorded as the average measured within each respective regions of interest.

TEM & IHC

After follow-up MRI studies, the mice were immediately euthanized and tumors excised. Each tumor was bisected to produce two approximately equal-sized tumor tissue samples.

The first half of the tumor sample was examined with TEM (Field Emission Inc., OR, USA). For TEM sample processing, small pieces of tumor tissue specimens (~0.5 mm^3 in size)

were placed into glutaraldehyde and fixed for 1 h at room temperature and then placed in osmium tetroxide. These fixed tissue samples were then embedded in agar for further processing. The specimens were dehydrated in graded concentrations of ethanol and propylene oxide and embedded in Spurr's plastic. Semi-thin (5 μm) sections were cut from the resulting block; thin sections (1.5 μm) were cut from these blocks and placed upon copper grids. Finally, these thin sections were examined with TEM techniques, producing digital images at 400–4900× magnification. Apoptotic cells were identified in these images based upon well-established morphologic criteria (e.g., cell shrinkage, chromatin condensation and margination, and apoptotic bodies). For each sample, four 600× fields were evaluated; within these fields, the total number of tumor cells and endothelial cells were counted along with the total number of apoptotic cells for both of these cell types. For each specimen we calculated an apoptosis index (AI) for both tumor and endothelial cells. Six sections were observed from each tumor using Equation 2:

$$\mathrm{AI}=\mathrm{apoptotic\ \ cells/total\ \ counted\ \ cells}\times 100\% \quad \text{(Equation 2)}$$

The reader (Z Zhang, who has 10 years experience interpreting TEM images) was blinded to independently review all images for quantitative analysis.

The second half of each gross tumor tissue specimen was fixed in 10% formalin, embedded in paraffin, and sliced (5-μm slice thickness). These slices were placed upon glass slides for hematoxylin and eosin staining; additional slices were fixed and stained using antibodies against cleaved caspase 3 (Biocare Medical, CA, USA) and terminal deoxynucleotidyl transferase dUTP nick-end labeling (TUNEL; BD Pharmingen, CA, USA) assays [31,32]. For each specimen, TUNEL and caspase 3 slides (specimens from central slices in both control tumors and IRE-treated tumors) were scanned at 20× magnification and digitized using the TissueFAXS system (TissueGnostics, CA, USA). HistoQuest® cell analysis software (TissueGnostics) was then used for automated measurement of the positive staining of cells within each slide (positively stained cells considered apoptotic). The total number of tumor cells was also measured and, finally, AI was calculated similarly to prior TEM studies, and expressed as a ratio of apoptotic cells to total number of tumor cells within each slide. These IHC AI measurements were performed for both TUNEL and caspase 3 slides.

Statistical analysis

ADC measurements as well as TEM and IHC AI measurements were expressed as mean ± standard deviation. One-way analysis of variance was used to compare: TEM-based measurements of AI in control and IRE-treated tumors for both tumor and endothelial cells; IHC IA measurements in control and IRE-treated tumors; and DW-MRI ADC measurements in control tumors and IRE-treated tumors before and after therapy (latter comparison included Tukey *post hoc* correction). Pearson correlation coefficients were calculated to:

- Assess the relationship between MRI ΔADC biomarker (ΔADC = tumor ADC post-IRE - tumor ADC at baseline) and corresponding IHC AI measurements in treated tumors

- Compare differences between control and IRE-treated IHC measurements performed separately for TUNEL and caspase 3 assays in each animal (i.e., comparing ΔIA TUNEL = IATUNEL post-IRE – IATUNEL control with AIA caspase 3 = IA caspase 3 post-IRE - IA caspase 3 control).

All statistical analyses were performed with Stata® software (Stata 11; Stata-Corp, TX, USA). Statistical significance was defined as $p < 0.05$.

Results

All 14 animals survived to completion of the designated procedure without any complications.

Histology

Hematoxylin and eosin slides from post-IRE tumor specimens demonstrated acute coagulative necrosis throughout the treated tumor volume; cell outlines remained with cell size unchanged compared with controls. Thrombosis was evident throughout the IRE-treated tumor specimen, with minimal thrombosis observed in control slices. Representative hematoxylin and eosin slides are shown at 4× magnifications (figure 1A, control; and Figure 1b, post-IRE) and at 200× magnification (Figure 1C, control; and Figure 1D, post-IRE). At 200× magnification, apoptotic cells could be identified based upon morphological criteria such as chromatin condensation and margination, and apoptotic bodies.

TEM

Morphologic characteristics of apoptosis were not observed within control tumor specimens; representative TEM images from control tumors are shown in Figures 2A & 2B Conversely, IRE-treated tumors demonstrated marked chromatin condensation, a classic hallmark of apoptosis; a representative TEM image from an IRE-treated tumor specimen is shown in Figure 2C Apoptotic bodies were also observed as tightly packed organelles within the cytoplasm (Figure 2C). Within the TEM image of an individual apoptotic tumor cell in Figure 2D, condensed chromatin was observed as sharply marginated electron-dense masses abutted to the nuclear envelope. Alterations of the cell membrane and organelles were observed as well as nanoscale defects/pores in both cellular and nuclear membranes; representative images shown in Figures 2D & 2E Microvessel endothelial cell apoptosis and microvessel thromboses were clearly observed in each treated specimen (Figures 2C & 2F). According to TEM assessments, the AI for control tumor cells was measured to be 4.6 ± 2.7% (n = eight tumors). AI for IRE-treated tumor tissue cells was significantly higher at 28.2 ± 9.9% (n = 20 tumors; $p = 0.002$). AI for microvessel endothelial cells was 20.8 ± 3.4% for IRE-treated specimens but significantly lower (3.2 ± 0.8%) for control tumor specimens ($p = 0.002$) (Figure 3).

IHC

Representative TUNEL and caspase 3 slides from PANC-1 xenograft tumors are shown in Figures 4A–4D; negligible signs of apoptosis were detected in control tumors (figure 4A, TUNEL; Figure 4B, caspase 3). Apoptosis was clearly indicated within TUNEL and caspase

3 slides from post-IRE tumor specimens (figure 4C, TUNEL; Figure 4D, caspase 3). The Al that was determined using these two separate IHC markers, demonstrated a similar pattern; significantly higher Al was measured in post-IRE tumor specimens than in control tumor specimens (Figure 4E). For the TUNEL assay, the AIs calculated for control tumors and IRE-treated tumors were 1.65 ± 0.76% and 22.53 ± 9.93%, respectively ($p = 0.001$). For caspase 3 method, the AIs calculated for control tumors and IRE-treated tumors were 3.83 ± 0.97% and 37.89 ± 15.12%, respectively ($p = 0.008$). There was a strong correlation between the ΔAI (the difference between the control and the treated tumor IHC markers within individual animals) calculated based upon TUNEL and caspase 3 approaches ($R = 0.71$) (Figure 4F).

MRI

Representative DW images of PANC-1 tumors from two representative animals are shown in Figure 5 Mean tumor ADC values increased after IRE treatment (control tumors: ADC = 654.45 ± 70.70 × 10^{-3} mm^2/s; treatment group tumors pre-IRE: ADC = 683.45 ± 75.12 × 10^{-3} mm^2/s, post-IRE; ADC = 820.2 ± 44.96 × 10^{-3} mm^2/s). ADC increases post-IRE were statistically significant ($p = 0.001$); conversely, there was not a significant difference between ADC values measured in control and treated tumors prior to IRE ($p = 0.35$). There was a strong correlation between ADC increases following IRE (ΔADC = difference between pre- and post-IRE ADC values) and follow-up TUNEL ($R = 0.78$) and caspase 3 AI measurements ($R = 0.83$) (Figure 6).

Discussion

The purpose of our study was to elucidate the subcellular morphological and structural alterations that occur immediately following IRE ablation and compare quantitative IHC measurements with an *in vivo* imaging assay indicative of nanoscale pore formation within the targeted tumor tissues. However, post-IRE MRI study took 30 min. Therefore, this time point was chosen in our study for IHC measurements. IRE induced rapid dramatic alterations to the tumor microstructure exhibited as chromatin condensation, formation of apoptotic bodies, and the presence of nanoscale defects in both cellular and nuclear membranes. IHC AI measurements increased significantly after IRE ablation; these IHC measurements were strongly correlated to quantitative MRI-based measurements of water-mobility increases immediately after the IRE procedure.

Several prior reversible electroporation (RE) studies showed that RE with low voltage creates crater-shaped nanopores in the electroporated human red blood cell membrane using SEM [18,33]. As expected in RE, these nanopores disappeared within 20 min of electroporation showing their transient nature [18]. Recently, RE and IRE responses were investigated using system models of both single cells and multiple cells. Models such as these can be highly valuable for interpreting the results of *in vivo* RE and IRE studies [34]. However, no study has been performed to visualize the ultrastructural changes and nanopore formation in an entire cell induced by high-voltage IRE. Recently, IRE studies have also utilized SEM methods to visualize cell membrane nanopore formation after tissue ablation procedures [17,20], but SEM does not permit observations of subcellular alterations to

internal structures. For our study in PDAC xenografts, TEM was alternatively used to permit these observations of alterations to the cell membrane, internal cell structures and organelles. Our TEM studies demonstrated rapid changes in morphologic characteristics following IRE, which is suggestive of apoptosis, along with a near complete obliteration of both cellular and nuclear membranes within the ablated tumor tissues.

Follow-up IHC studies were highly concordant, demonstrating significant increases in caspase 3 and TUNEL staining within IRE-ablated tumor tissues. These rapid alterations to the tumor microstructure occurred within 30 min, including the delay period to tissue harvest necessary to complete follow-up post-IRE imaging studies. In addition, the tissue sections were taken from a single section of each tumor. Tweezer-style electrodes were used for these studies to produce a relatively homogenous electrical field (disk electrodes with diameters larger than the treated tumor) [35]. However, the induced fields were not measured and it remains possible that different positions within each tumor experienced different field strengths.

Recent hepatic IRE studies reported that large vessel endothelial cells may be protected from IRE-induced ablation within *in vivo* procedural settings. In normal liver tissue, IRE ablation zones traversed large vessels and bile ducts without damaging these vital structures [20]. However, our TEM studies in PDAC xenografts demonstrated that IRE induces apoptosis of tumor endothelial cells. This microvasculature disruption could conceivably play an important role in overall tissue response following IRE procedures, particularly when additionally considering the concurrent thrombosis widely observed within the ablated tissue volume. In this study, all animals were immediately euthanized at a 30-min follow-up interval to perform histologic, IHC and TEM examinations. IRE parameters were selected such that the electrical fields induced should ultimately ablate these tumor tissues [20,21,36], and would therefore be anticipated to produce positive outcomes (stabilization and/or elimination as suggested). Positive longitudinal response has also been demonstrated in our prior studies [36–39]; the purpose of this work focused on microstructural changes shortly after IRE ablation procedures.

Prior studies have qualitatively demonstrated increases in IHC apoptosis markers (e.g., BAX, TUNEL, caspase 3 and BCL-2) following IRE procedures in porcine liver tissues, rat vascular smooth muscle cells and rat hepatocellular carcinoma xenografts [20,36,40,41]. For current PDAC xenograft study, our quantitative IHC measurements (performed using rigorous AI calculations) were consistent with these earlier fndings. Both TUNEL and caspase 3 AI measurements increased significantly within 30 min following completion of the IRE procedure. These consistent observations of dramatic life-cycle alterations over such a short time scale are relatively unprecedented. While a broad spectrum of both targeted and systemic therapies attempt to induce apoptosis as a primary therapeutic mechanism, to our knowledge none exhibit such rapid alterations.

The DW-MRI approach is a highly sensitive tool that has demonstrated the potential to serve as an *in vivo* biomarker for early detection of tumor response prior to anatomic tumor size changes [36,42–46]. Significant changes in tumor tissue water mobility have been detected in breast, brain, prostate and GI tract tumors following radiation and/or chemotherapy

[36,42–46]. For the aforementioned studies, water mobility changes were attributed to tissue microstructural alterations during either necrosis or apoptotic cell-death pathways. Our study has demonstrated that cells within the IRE-treated tissues ultimately enter coagulative necrosis and the apoptotic cell-death pathway [19–21] ; therefore, the DW-MRI method should be sensitive to assess IRE response in tumor.

Our results showed that significant increases in water diffusion (ADC) were detected within 30 min of ablation procedure completion and DW-magnetic resonance images showed the reduction in signal intensity within DW images following IRE for both tumors indicative of diffusion (water mobility) increases with these tissues immediately following IRE ablation in each tumor. ADC biomarker can be critical to permit early adjustments to IRE therapeutic regimens, either retreatment with prior intervention or adoption of alternative treatment strategies. In this study, rapidly structural and morphological alterations along with significantly elevated apoptosis markers were consistently observed and well correlated to ADC measurements. However, this correlation between apoptosis measurement and ADC value does not necessarily imply causation. Future studies should test the sensitivity of the gradation of ADC changes with changing IRE ablation parameters in order to identify rigorous thresholds for accurately predicting treatment response [28].

These findings were consistent with observed structural alterations (TEM findings) and strongly correlated to corresponding IHC AI measurements. Given that IHC measurements are not generally feasible in clinical settings, this imaging assay could be highly valuable for the detection of tumor response following IRE ablation. These noninvasive imaging techniques should permit rapid prediction of treatment outcomes to facilitate patient-specific adjustments to the treatment protocol. Future studies are clearly warranted to investigate the efficacy of these DW-MRI techniques in clinical settings of IRE tumor ablation.

The current study had several limitations. First, our study was designed so that IRE ablation parameters were selected to completely treat the targeted tumors [20,21,36]. TEM, IHC and MRI was performed at only a single, early time point after IRE ablation. Future serial studies, while significantly increasing logistical complexity, could also be valuable to investigate the extended time course of microstructure changes following IRE ablation. The latter studies could be particularly valuable in those clinical settings wherein early follow-up imaging intervals (<30 min post-IRE) are not feasible. Second, IHC, TEM and MRI assays were only compared between control and treated tumors (as opposed to comparing different positions within the same tumor) due to complete ablation of treated tumors in our current study. The latter approach was adopted to avoid the need for rigorous coregistration between IRE electrode positions and tumor tissues specimens. Nonetheless, while our approach avoided ambiguities and confounding outcomes that can result from poor registration, investigation of the intratumoral variability of these IHC, TEM and imaging findings could be quite valuable. Future clinical translation of these MRI techniques for IRE monitoring applications will require additional investigations. Specifically, it will be valuable to determine the gradation of ADC changes that occur with changing IRE ablation parameters in order to identify rigorous thresholds for accurately predicting treatment response. Ultimately, while the current study used pulsing parameters of 64 pulses at 100 ms spacing, these may not be appropriate in clinical settings. Clinical protocols for IRE ablation

typically involve synchronization of pulse application with the heart beat, therefore using an inter-pulse spacing of approximately 1 s.

IRE is an innovative, newly available ablation technology offering multiple potential benefits over alternative thermal ablation approaches [22,47,48]. Thermal ablation leads to coagulative necrosis within the targeted tumor volume. Via a vastly different therapeutic mechanism, IRE alternatively leads to tissue destruction through targeted induction of apoptosis. Our preclinical IRE studies in the PDAC xenograft mouse model demonstrate rapid, dramatic alterations to the tumor microstructure shortly after IRE. Significant structural and morphological alterations were clearly evident and apoptosis markers were significantly elevated compared with nontreated controls. These findings were well correlated with DW-MRI measurements, thus suggesting that *in vivo* imaging assays may one day serve as *in vivo* biomarkers for noninvasive detection of tumor response.

Acknowledgments

Special thanks to D-HKim for assistance with transmission electron microscopy studies. We also thank J Nicolai for cell culture support.

This work was supported by American Cancer Society SP0011492 (Z Zhang), National Cancer Institute CA134719 (AC Larson), and funds from the NIH Clinical and Translational Science Awards Program (Northwestern University, IL, USA; UL1RR0254741).

References

1. Jemal A, Siegel R, Ward E, Hao Y, Xu J, Thun MJ. Cancer statistics, 2009. CA Cancer J. Clin. 2009; 59(4):225–249. [PubMed: 19474385]
2. Olive KP, Jacobetz MA, Davidson CJ, et al. Inhibition of Hedgehog signaling enhances delivery of chemotherapy in a mouse model of pancreatic cancer. Science. 2009; 324(5933):1457–1461. [PubMed: 19460966]
3. Lencioni R. Loco-regional treatment of hepatocellular carcinoma. Hepatology. 2010; 52(2):762–773. [PubMed: 20564355]
4. Kulke MH, Siu LL, Tepper JE, et al. Future directions in the treatment of neuroendocrine tumors: consensus report of the National Cancer Institute Neuroendocrine Tumor clinical trials planning meeting. J. Clin. Oncol. 2011; 29(7):934–943. [PubMed: 21263089]
5. Willett CG, Czito BG, Bendell JC, Ryan DP. Locally advanced pancreatic cancer. J. Clin. Oncol. 2005; 23(20):4538–4544. [PubMed: 16002845]
6. Miller L, Leor J, Rubinsky B. Cancer cells ablation with irreversible electroporation. Technol. Cancer Res. Treat. 2005; 4(6):699–705. [PubMed: 16292891]
7. Iida N, Nakamoto Y, Baba T, et al. Antitumor effect after radiofrequency ablation of murine hepatoma is augmented by an active variant of CC Chemokine ligand 3/macrophage inflammatory protein-lalpha. Cancer Res. 2010; 70(16):6556–6565. [PubMed: 20663902]
8. Meza-Junco J, Montano-Loza AJ, Liu DM, et al. Locoregional radiological treatment for hepatocellular carcinoma; which, when and how? Cancer Treat. Rev. 2012; 38(1):54–62. [PubMed: 21726960]
9. Goldberg SN, Grassi CJ, Cardella JF, et al. Image-guided tumor ablation: standardization of terminology and reporting criteria. Radiology. 2005; 235(3):728–739. [PubMed: 15845798]
10. Brace CL, Hinshaw JL, Lubner MG. Thermal ablation for the treatment of abdominal tumors. J. Vis. Exp. 2011; 7(49):2596. [PubMed: 21445029]
11. Phillips M, Maor E, Rubinsky B. Nonthermal irreversible electroporation for tissue decellularization. J. Biomech. Eng. 2010; 132(9):091003. [PubMed: 20815637]

12. Rubinsky B. Irreversible electroporation in medicine. Technol. Cancer Res. Treat. 2007; 6(4):255–260. [PubMed: 17668932]
13. Rubinsky B, Onik G, Mikus P. Irreversible electroporation: a new ablation modality -clinical implications. Technol. Cancer Res. Treat. 2007; 6(1):37–48. [PubMed: 17241099]
14. Ahmed M, Brace CL, Lee FT Jr, Goldberg SN. Principles of and advances in percutaneous ablation. Radiology. 2011; 258(2):351–369. [PubMed: 21273519]
15. Griggs JJ, Somerfield MR, Anderson H, et al. American Society of Clinical Oncology endorsement of the cancer care Ontario practice guideline on adjuvant ovarian ablation in the treatment of premenopausal women with early-stage invasive breast cancer. J. Clin. Oncol. 2011; 29(29):3939–3942. [PubMed: 21900112]
16. Davalos RV, Mir IL, Rubinsky B. Tissue ablation with irreversible electroporation. Ann. Biomed. Eng. 2005; 33(2):223–231. [PubMed: 15771276]
17. Lee EW, Wong D, Prikhodko SV, et al. Electron microscopic demonstration and evaluation of irreversible electroporation-induced nanopores on hepatocyte membranes. J. Vasc. Interv. Radiol. 2012; 23(1):107–113. [PubMed: 22137466]
18. Chang DC, Reese TS. Changes in membrane structure induced by electroporation as revealed by rapid-freezing electron microscopy. Biophys. J. 1990; 58(1):1–12. [PubMed: 2383626]
19. Lee EW, Thai S, Kee ST. Irreversible electroporation: a novel image-guided cancer therapy. Gut liver. 2010; 4(Suppl. 1):S99–S104. [PubMed: 21103304]
20. Lee EW, Chen C, Prieto VE, Dry SM, Loh CT, Kee ST. Advanced hepatic ablation technique for creating complete cell death: irreversible electroporation. Radiology. 2010; 255(2):426–433. [PubMed: 20413755]
21. Golberg A, Rubinsky B. A statistical model for multidimensional irreversible electroporation cell death in tissue. Biomed. Eng. Online. 2010; 9(13):13. [PubMed: 20187951]
22. Edd JF, Horowitz L, Davalos RV, Mir LM, Rubinsky B. *In vivo* results of a new focal tissue ablation technique: irreversible electroporation. IEEE Trans. Biomed. Eng. 2006; 53(7):1409–1415. [PubMed: 16830945]
23. Daniels CS, Rubinsky B. Cryosurgery with pulsed electric fields. PIoS ONE. 2011; 6(11):e26219.
24. Garcia PA, Rossmeisl JH Jr, Neal RE 2nd, Ellis TL, Davalos RV. A parametric study delineating irreversible electroporation from thermal damage based on a minimally invasive intracranial procedure. Biomed. Eng. Online. 2011; 10(34):34. [PubMed: 21529373]
25. Sano MB, Neal RE 2nd, Garcia PA, Gerber D, Robertson J, Davalos RV. Towards the creation of decellularized organ constructs using irreversible electroporation and active mechanical perfusion. Biomed. Eng. Online. 2010; 9(83):83. [PubMed: 21143979]
26. Yang XJ, Li J, Sun CX, Zheng FY, Hu LN. The effect of high frequency steep pulsed electric fields on *in vitro* and *in vivo* antitumor efficiency of ovarian cancer cell line skov3 and potential use in electrochemotherapy. J. Exp. Clin. Cancer Res. 2009; 28(53):53. [PubMed: 19386105]
27. Spugnini EP, Arancia G, Porrello A, et al. Ultrastructural modifications of cell membranes induced by ‘electroporation’ on melanoma xenografts. Microsc. Res. Tech. 2007; 70(12):1041–1050. [PubMed: 17722056]
28. Mahmood F, Hansen RH, Agerholm-Larsen B, Jensen KS, Iversen HK, Gehl J. Diffusion-weighted MRI for verification of electroporation-based treatments. J. Membr. Biol. 2011; 240(3):131–138. [PubMed: 21380763]
29. Esser AT, Smith KC, Gowrishankar TR, Weaver JC. Towards solid tumor treatment by irreversible electroporation: intrinsic redistribution of fields and currents in tissue. Technol. Cancer Res. Treat. 2007; 6(4):261–274. [PubMed: 17668933]
30. Wang Z, Vemuri BC, Chen Y, Mareci T. A constrained variational principle for direct estimation and smoothing of the diffusion tensor field from DWI. Inf. Process Med. Imaging. 2003; 18:660–671. [PubMed: 15344496]
31. Roy SK, Chen Q, Fu J, Shankar S, Srivastava RK. Resveratrol inhibits growth of orthotopic pancreatic tumors through activation of FOXO transcription factors. PLoS ONE. 2011; 6(9):e25l66.
32. Cheng G, Zhu L, Mahato RI. caspase 3 gene silencing for inhibiting apoptosis in insulinoma cells and human islets. Mol. Pharm. 2008; 5(6):1093–1102. [PubMed: 18828606]

33. Lahijani MS, Tehrani DM, Sabouri E. Histopathological and ultrastructural studies on the effects of electromagnetic fields on the liver of preincubated white Leghorn chicken embryo. Electromagn. Biol. Med. 2009; 28(4):391–413. [PubMed: 20017630]
34. Gowrishankar TR, Esser AT, Smith KC, Son RS, Weaver JC. Intracellular electroporation site distributions: modeling examples for nsPEF and IRE pulse waveforms. Conf. Proc. IEEE Eng. Med. Biol. Soc. 2011; 2011:732–735. [PubMed: 22254414]
35. Edd JF, Davalos RV. Mathematical modeling of irreversible electroporation for treatment planning. Technol. Cancer Res. Treat. 2007; 6(4):275–286. [PubMed: 17668934]
36. Guo Y, Zhang Y, Klein R, et al. Irreversible electroporation therapy in the liver: longitudinal efficacy studies in a rat model of hepatocellular carcinoma. Cancer Res. 2010; 70(4):1555–1563. [PubMed: 20124486]
37. Guo Y, Zhang Y, Nijm GM, et al. Irreversible electroporation in the liver: contrast-enhanced inversion-recovery MR imaging approaches to differentiate reversibly electroporated penumbra from irreversibly electroporated ablation zones. Radiology. 2011; 258(2):461–468. [PubMed: 21131581]
38. Guo Y, Zhang Y, Jin N, et al. Electroporation-mediated transcatheter arterial chemoembolization in the rabbit VX2 liver tumor model. Invest. Radiol. 2012; 47(2):116–120. [PubMed: 21934518]
39. Zhang Y, Guo Y, Ragin AB, et al. MR imaging to assess immediate response to irreversible electroporation for targeted ablation of liver tissues: preclinical feasibility studies in a rodent model. Radiology. 2010; 256(2):424–432. [PubMed: 20656834]
40. Maor E, Ivorra A, Leor J, Rubinsky B. The effect of irreversible electroporation on blood vessels. Technol. Cancer Res. Treat. 2007; 6(4):307–312. [PubMed: 17668938]
41. Lee EW, Loh CT, Kee ST. Imaging guided percutaneous irreversible electroporation: ultrasound and immunohistological correlation. Technol. Cancer Res. Treat. 2007; 6(4):287–294. [PubMed: 17668935]
42. Jensen LR, Garzon B, Heldahl MG, Bathen TF, Lundgren S, Gribbestad IS. Diffusion-weighted and dynamic contrast-enhanced MRI in evaluation of early treatment effects during neoadjuvant chemotherapy in breast cancer patients. J. Magn. Reson. Imaging. 2011; 34(5):1099–1109. [PubMed: 22002757]
43. Morgan VA, Riches SF, Thomas K, et al. Diffusion-weighted magnetic resonance imaging for monitoring prostate cancer progression in patients managed by active surveillance. Br. J. Radiol. 2011; 84(997):31–37. [PubMed: 21172965]
44. Petralia G, Thoeny HC. DW-MRI of the urogenital tract: applications in oncology. Cancer Imaging. 2010; 10(Spec. no A):S112–S123. [PubMed: 20880781]
45. Pope WB, Qiao XJ, Kim HJ, et al. Apparent diffusion coefficient histogram analysis stratifies progression-free and overall survival in patients with recurrent GBM treated with bevacizumab: a multicenter study. J. Neurooncol. 2012; 108(3):491–498. [PubMed: 22426926]
46. Tang L, Zhang XP, Sun YS, et al. Gastrointestinal stromal tumors treated with imatinib mesylate: apparent diffusion coefficient in the evaluation of therapy response in patients. Radiology. 2011; 258(3):729–738. [PubMed: 21193597]
47. Bower M, Sherwood L, Li Y, Martin R. Irreversible electroporation of the pancreas: definitive local therapy without systemic effects. J. Surg. Oncol. 2011; 104(1):22–28. [PubMed: 21360714]
48. Breton M, Mir LM. Microsecond and nanosecond electric pulses in cancer treatments. Bioelectromagnetics. 2012; 33(2):106–123.

Executive summary

Irreversible electroporation for therapy

- NanoKnife® (Angiodynamics, Inc., NY, USA) or irreversible electroporation (IRE) induces the formation of nanopores within the eel membrane, leading to rapid dramatic alterations to the tumor microenvironment.
- Cells within the IRE-treated tissues ultimately enter coagulative necrosis and the apoptotic cell-death pathway.

Diffusion-weighted MRI can monitor the ultrastructural changes following IRE tumor ablation

- MRI permits noninvasive quantitative measurements of rapid dramatic alterations to the tumor microenvironment following IRE ablation.
- MRI biomarkers can monitor early therapy response of NanoKnife ablation, which will permit rapid, timely adoption of alternative treatment strategies (IRE parameters) in clinical application.

Future perspective

- IRE for tumor ablation is still in the developmental stages, although the safety and therapeutic efficacy of these methods have been well established in animal models.
- Additional ongoing studies are necessary to fully evaluate safety and efficacy in clinical settings.
- Image-guided IRE monitoring techniques should be valuable to permit patient-specific protocol optimization, early detection of response and timely adoption of alternative treatment strategies when necessary.

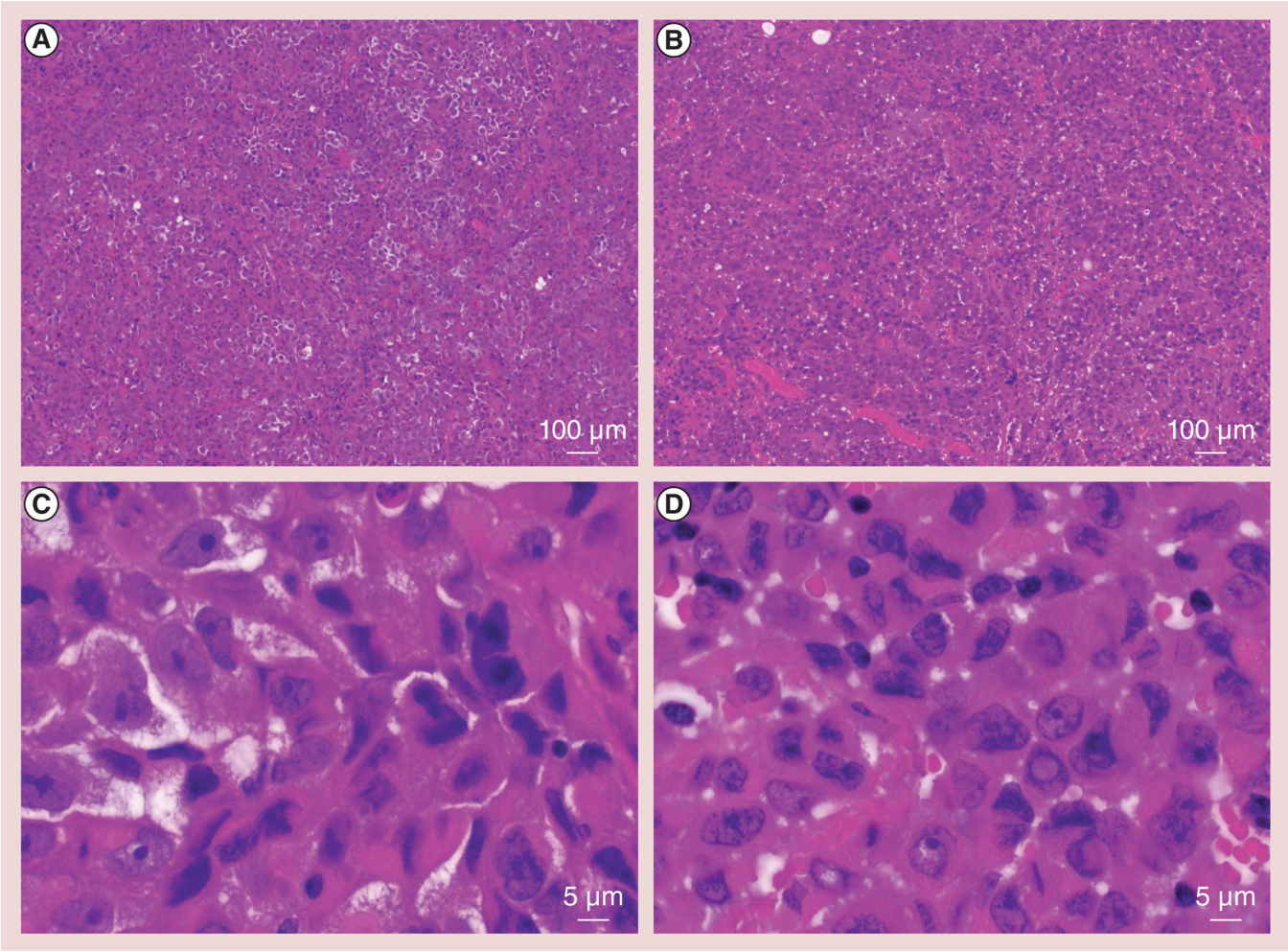

Figure 1. Representative hematoxylin and eosin slides from control and following 30 min of irreversible electroporation-treated tumors

(A) Control tumor and **(B)** irreversible electroporation (IRE)-treated tumor at low magnification (4×). Post-IRE tumor specimens demonstrated acute coagulative necrosis. **(C)** Control tumor and **(D)** IRE-treated tumor at high magnification (200×). Apoptotic cells within the post-IRE tumor specimen were identified according to morphological criteria including chromatin condensation and margination, and apoptotic bodies. Significant levels of microvessel thrombosis were observed in post-IRE specimens.

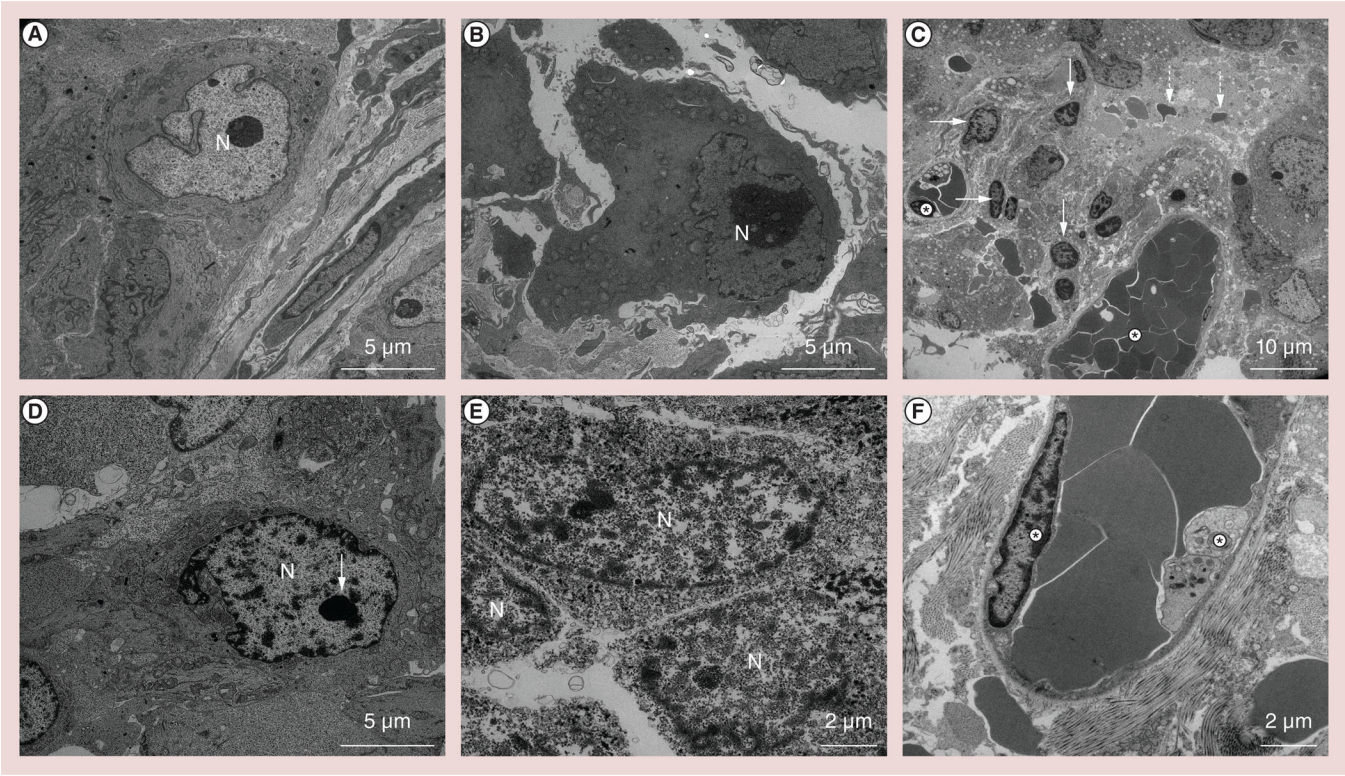

Figure 2. Representative transmission electron microscopy slides from the control and following 30 min of irreversible electroporation-treated tumor specimens

Morphological characteristics of apoptosis were not readily observed in **(A & B)** control tumor specimens. In irreversible electroporation-treated specimens, marked chromatin condensation was observed with chromatin abutment to the nuclear envelope (arrows); apoptotic bodies (dashed arrows) were clearly observed throughout **(C & D)** treated specimens. **(E)** Transmission electron microscopy permitted direct observation of the significant alterations of the cell membrane and organelles along with nanoscale defects and pore formation in both cellular and nuclear membranes. **(C & F)** At high magnification, morphologic hallmarks of apoptosis were also observed within microvessel endothelial cells (asterisks).

N: Nucleus.

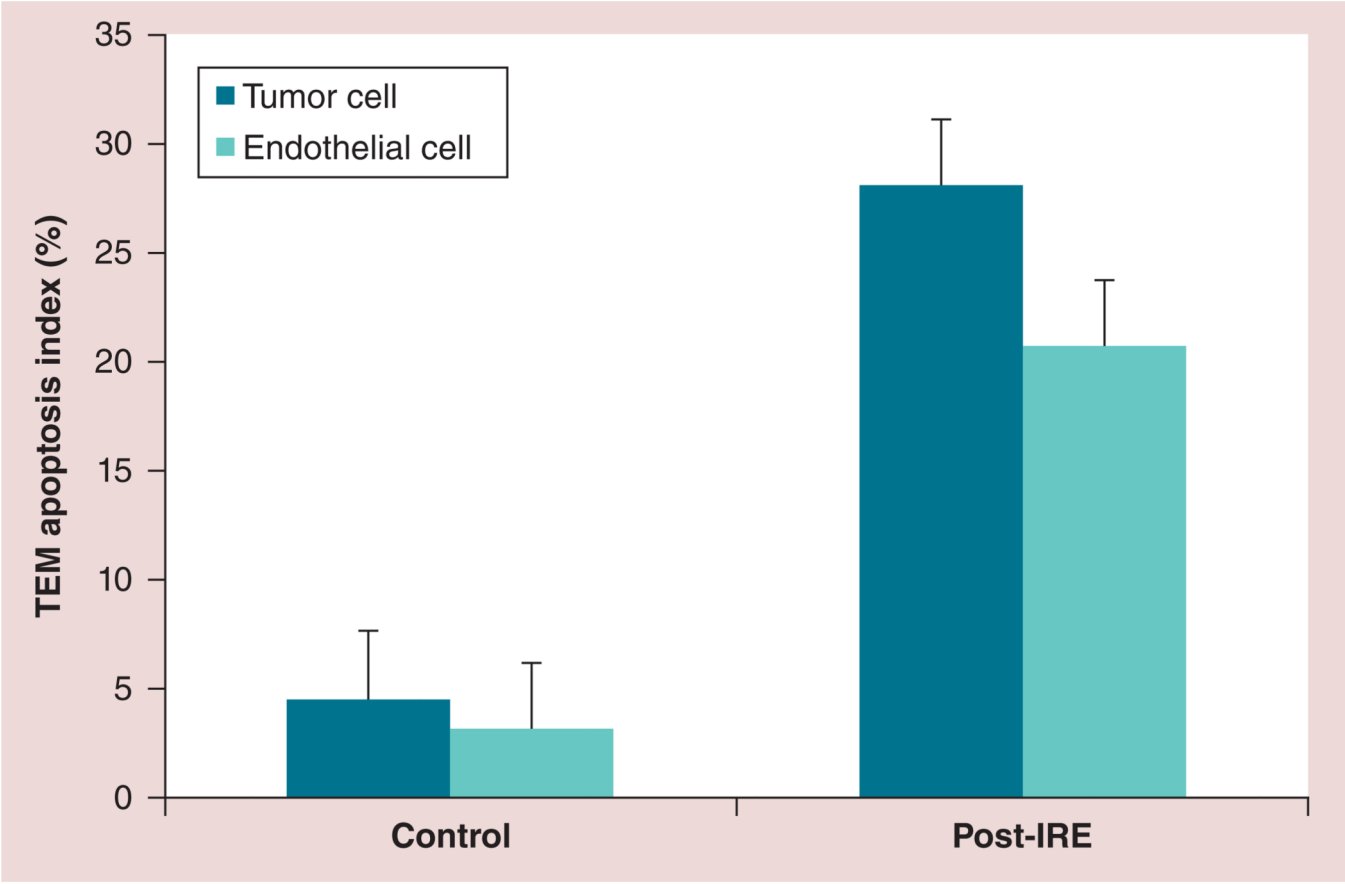

Figure 3. Transmission electron microscopy apoptosis index measurements for the control and following 30 min of irreversible electroporation-treated tumor specimens

Six sections were observed from each tumor. Significantly increased apoptosis index was observed for both tumor cells and endothelial cells within IRE-treated tumor specimens (both $p = 0.002$). Error bars represent the standard deviations.

IRE: Irreversible electroporation; TEM: Transmission electron microscopy.

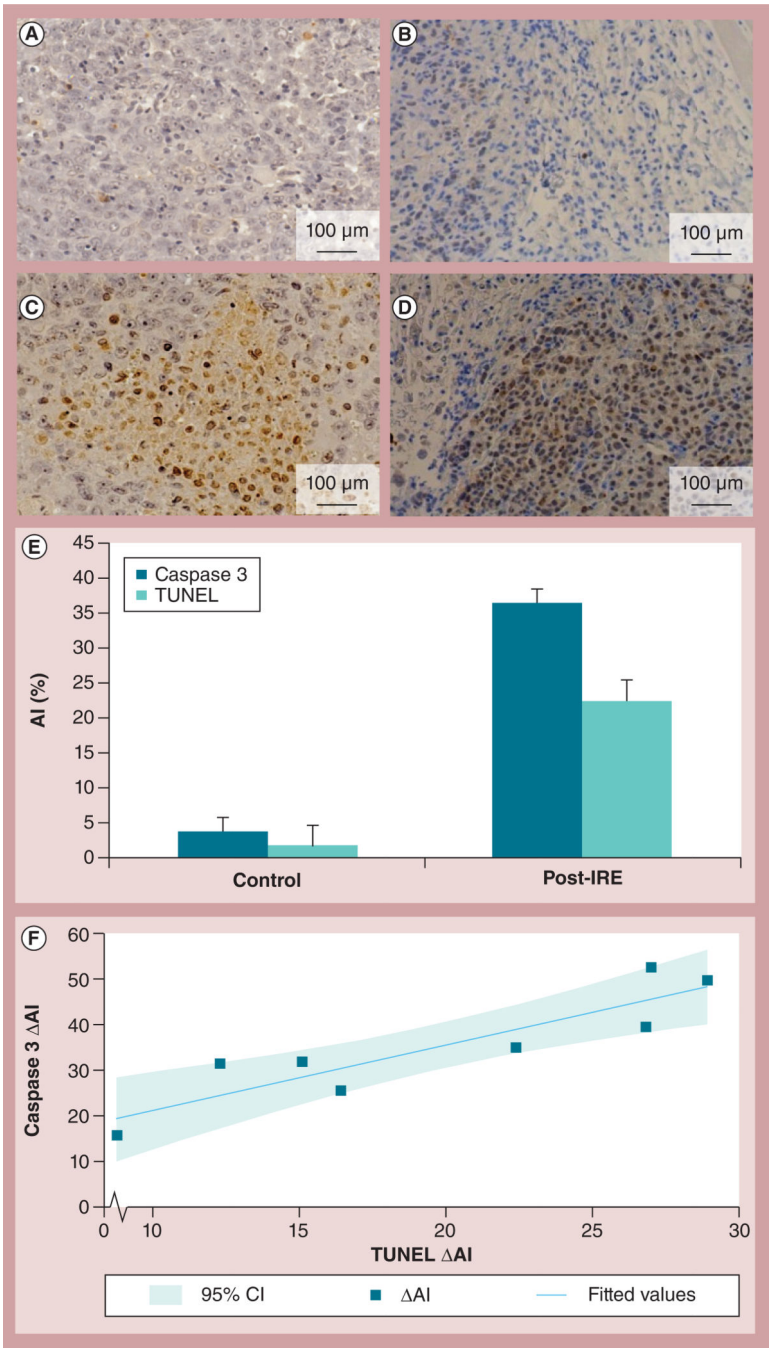

Figure 4. TUNEL and caspase 3 slides from both control and irreversible electroporation-treated tumors

IRE-induced significant levels of apoptosis were verified by TUNEL assay **([A]** the control tumor and **[C]** the IRE-treated tumor) and cleaved caspase 3 (**[B]** the control tumor and **[D]** the IRE-treated tumor). **(E)** Al was significantly increased in the IRE-treated tumor specimens compared with the control as assessed with both immunohistochemistry methods (TUNEL, p = 0.001; caspase 3, p = 0.008). Error bars represent the standard deviations. **(F)**

A strong correlation was observed between ΔAI (difference between control and treated tumor markers in each rat) calculated from TUNEL and caspase 3 measurements, R = 0.71. Al: Apoptosis index; IRE: Irreversible electroporation; TUNEL: Terminal deoxynucleotidyl transferase dUTP nick-end labeling.

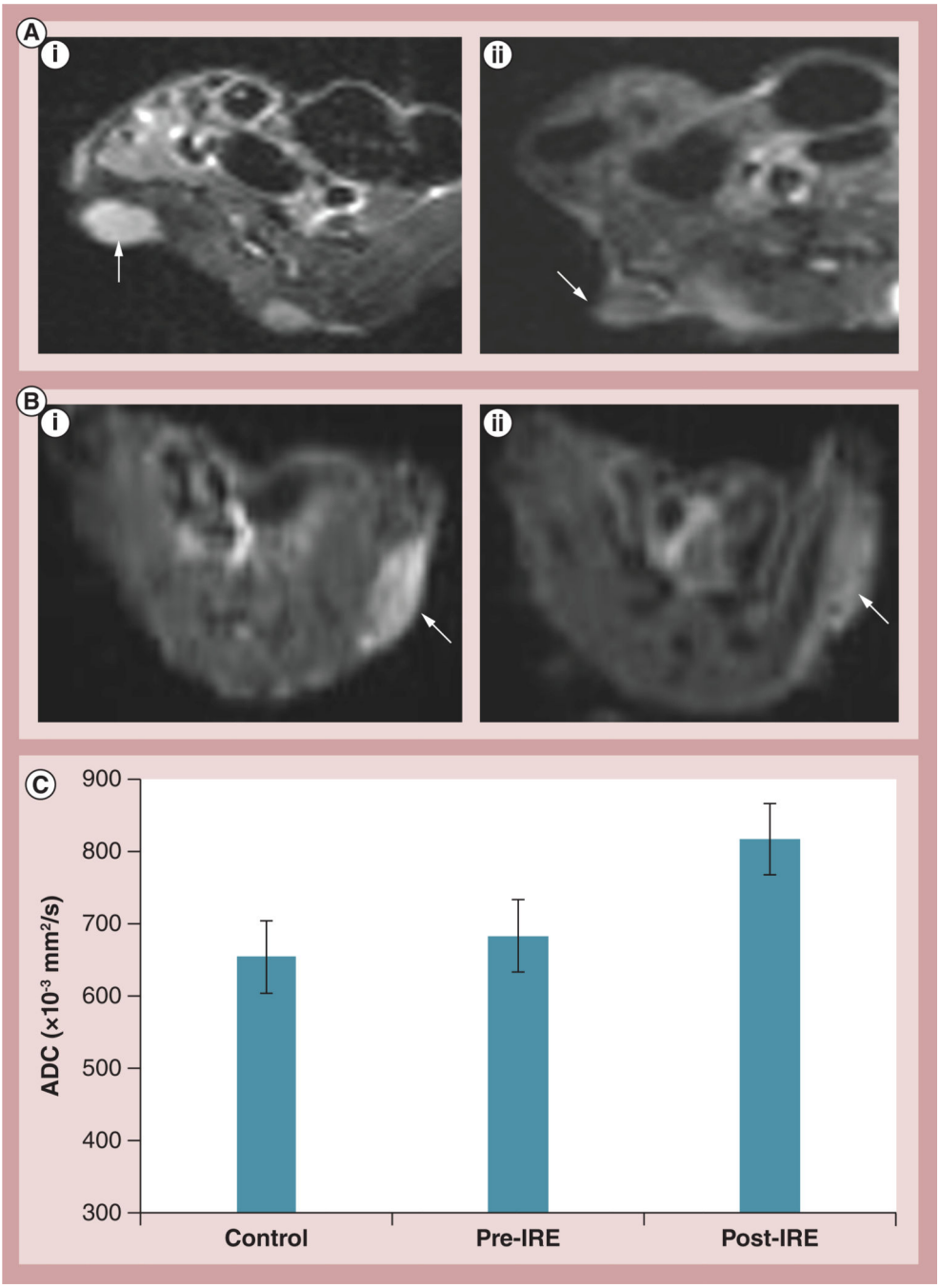

Figure 5. Representative diffusion-weighted magnetic resonance images

(A & B) Axial diffusion-weighted magnetic resonance images (b = 500 s/mm^2) of PANC-1 xenograft tumors (arrows) in two representative animals (rat A and rat B) **(A,i & B,i)** before and **(A,ii** & **B,ii)** after IRE. Notice reduction in signal intensity within diffusion-weighted images following IRE for both tumors indicative of diffusion (water mobility) increases with these tissues immediately following IRE ablation. Quantitative apparent diffusion coefficient values were significantly higher in these tumor tissues following IRE ablation (p = 0.001); **(C)** there was no significant difference between ADC values measured in control

tumors and treatment group tumors immediately prior to IRE ($p = 0.05$). Error bars represent the standard deviations.

ADC: Apparent diffusion coefficient; IRE: Irreversible electroporation.

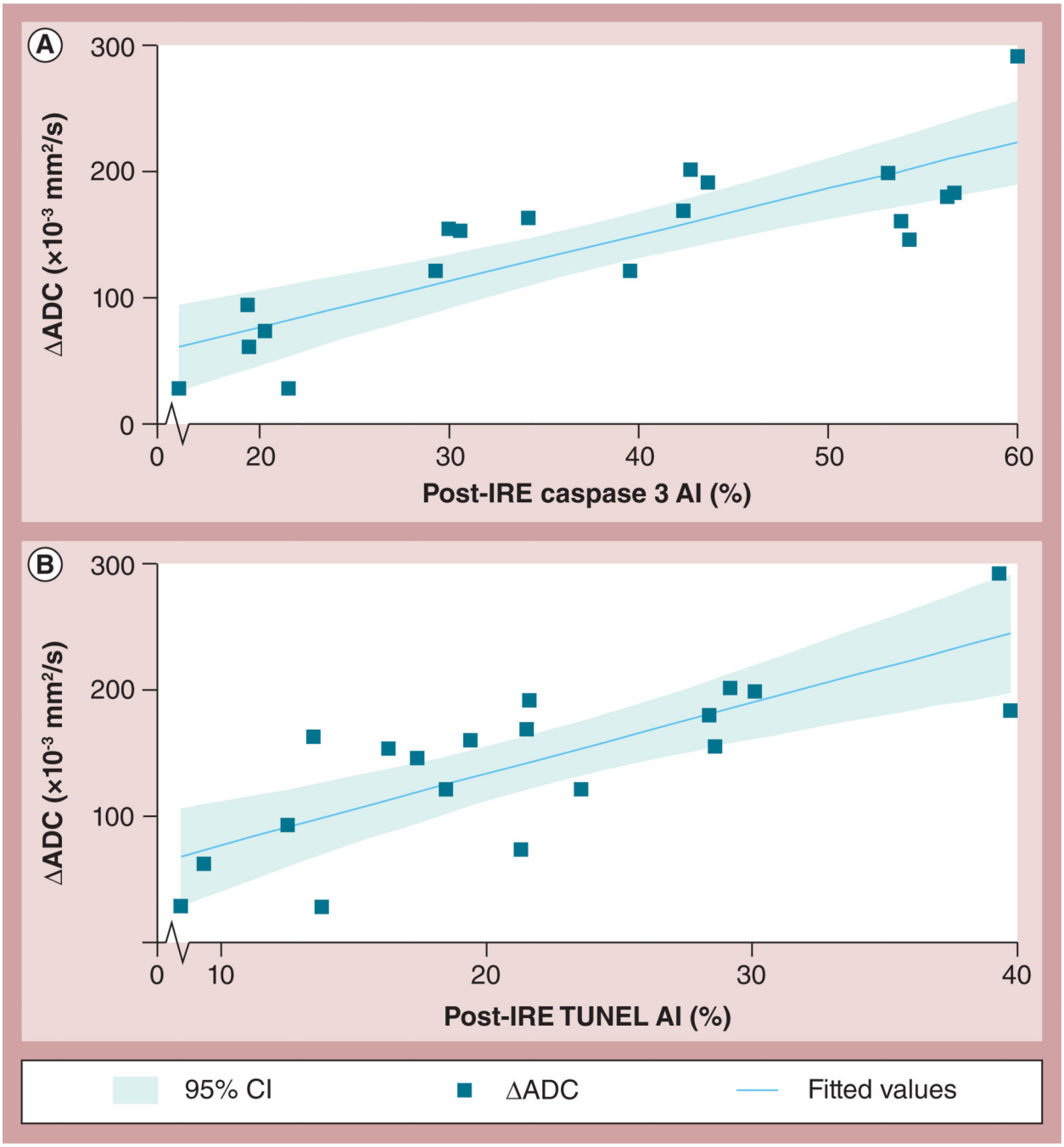

Figure 6. Comparison between immunohistochemistry markers of tumor apoptosis (TUNEL and caspase 3) and apparent diffusion coefficient changes following irreversible electroporation ablation procedures in PANC-1 xenograft tumors changes

The apoptosis index was evaluated by the detection of different molecular pathway methods including **(A)** caspase 3 and **(B)** TUNEL; however, a strong correlation was observed between these ADC and IHC measurements (caspase 3 assay: R = 0.83; and TUNEL: R = 0.78).

ADC: Apparent diffusion coefficient; AI: Apoptosis index; IRE: Irreversible electroporation; TUNEL: Terminal deoxynucleotidyl transferase dUTP nick-end labeling.